Parametric investigation of railway fastenings into the formation and mitigation of short pitch corrugation

Zhang, Pan; Li, Shaoguang; Dollevoet, Rolf; Li, Zili

DOI
10.1007/s40534-024-00332-w

Publication date
2024

Document Version
Final published version

Published in
Railway Engineering Science

Citation (APA)
Zhang, P., Li, S., Dollevoet, R., & Li, Z. (2024). Parametric investigation of railway fastenings into the formation and mitigation of short pitch corrugation. *Railway Engineering Science*, *32*(3), 286-306. https://doi.org/10.1007/s40534-024-00332-w

Railway Engineering Science
https://doi.org/10.1007/s40534-024-00332-w

Parametric investigation of railway fastenings into the formation and mitigation of short pitch corrugation

Pan Zhang[1] · Shaoguang Li[1] · Rolf Dollevoet[1] · Zili Li[1]

Received: 31 July 2023 / Revised: 17 January 2024 / Accepted: 17 January 2024

Abstract
Short pitch corrugation has been a problem for railways worldwide over one century. In this paper, a parametric investigation of fastenings is conducted to understand the corrugation formation mechanism and gain insights into corrugation mitigation. A three-dimensional finite element vehicle–track dynamic interaction model is employed, which considers the coupling between the structural dynamics and the contact mechanics, while the damage mechanism is assumed to be differential wear. Various fastening models with different configurations, boundary conditions, and parameters of stiffness and damping are built up and analysed. These models may represent different service stages of fastenings in the field. Besides, the effect of train speeds on corrugation features is studied. The results indicate: (1) Fastening parameters and modelling play an important role in corrugation formation. (2) The fastening longitudinal constraint to the rail is the major factor that determines the corrugation formation. The fastening vertical and lateral constraints influence corrugation features in terms of spatial distribution and wavelength components. (3) The strengthening of fastening constraints in the longitudinal dimension helps to mitigate corrugation. Meanwhile, the inner fastening constraint in the lateral direction is necessary for corrugation alleviation. (4) The increase in fastening longitudinal stiffness and damping can reduce the vibration amplitudes of longitudinal compression modes and thus reduce the track corrugation propensity. The simulation in this work can well explain the field corrugation in terms of the occurrence possibility and major wavelength components. It can also explain the field data with respect to the small variation between the corrugation wavelength and train speed, which is caused by frequency selection and jump between rail longitudinal compression modes.

Keywords Short pitch corrugation · Fastening modelling and parameters · Corrugation formation and mitigation · Rail longitudinal compression modes · Finite element vehicle–track interaction model

1 Introduction

Short pitch corrugation (referred to as corrugation hereinafter) is a (quasi-) periodic rail head defect that is recognised by shining peaks and dark troughs (see Fig. 1). Corrugation typically falls in the wavelength range of 20–80 mm with amplitude up to 100 μm and mainly occurs on straight tracks or gentle curves [1]. Corrugation excites large wheel–rail impact forces, accelerating the deterioration of track components and inducing rolling contact fatigue, such as squats [2]. Besides, a high level of 'roaring' noise generated by corrugation is a nuisance to passengers and residents near railway lines [3, 4]. Although corrugation has been a problem for railway managers worldwide for over a century, there has been no ultimate countermeasure against it so far. The most efficient and reliable solution is rail grinding. However, grinding increases the maintenance cost and also reduces the railway network availability. Therefore, it is essential to understand the corrugation formation mechanism and find effective solutions.

The mechanism of corrugation formation is generally considered to consist of two features: the wavelength-fixing mechanism and the damage mechanism [1]. The damage mechanism is commonly assumed to be wear [5–11], while a widely accepted wavelength-fixing mechanism has not been proposed. Pinned–pinned resonance, where rail vibrates with the wavelength of two sleeper spans, is often attributed to the corrugation wavelength-fixing mechanism [12–15]. Nevertheless, one difficulty with this mechanism

✉ Zili Li
Z.Li@tudelft.nl

[1] Section of Railway Engineering, Delft University of Technology, Stevinweg 1, 2628 CN Delft, the Netherlands

Published online: 17 March 2024

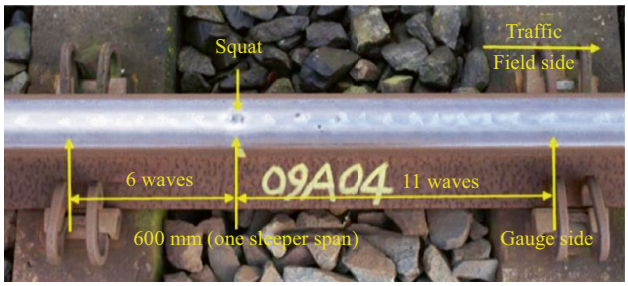

Fig. 1 Short pitch corrugation with a wavelength of about 35 mm. The squat was induced by corrugation and occurred at around 1/3 sleeper span. The photo was taken near Steenwijk, the Netherlands

is that it cannot easily explain the relatively small variation of corrugation wavelength with train speed [16]. Additionally, according to this mechanism, corrugation may occur everywhere above the sleeper support after a certain amount of train passages, and the embedded rail system that eliminates pinned–pinned modes should be corrugation-free, which are both not the case in practice [17]. Some researchers studied the multiple wheelset–rail dynamic interactions and reported that the local vertical rail bending modes between two wheels are responsible for corrugation formation [18–20]. Except for the vertical dynamics, the simulation results [13, 21] indicated that the lateral track dynamics may also play an important role in corrugation development.

Recently, new insights have been gained into the corrugation development mechanism employing a three-dimensional (3D) finite element (FE) wheel–track dynamic interaction model [22–24]. Corrugation was successfully reproduced using this model, which shared features similar to the field corrugation in terms of spatial distribution and the major wavelength component. The numerical simulation results indicated that rail longitudinal vibration modes are dominant for corrugation initiation with necessary initial excitation from the degraded fastenings [22, 23]. To verify this new finding, an innovative downscale vehicle–track interaction test rig named 'V-Track' was used to perform the corrugation experiment under the loading conditions similar to those on straight tracks. Some fastening clamps were loosened in the V-Track to simulate fastening degradation, and rail corrugation was successfully produced [25]. The experimental results agree with the numerical simulation, and both show that rail longitudinal vibration mode and its induced longitudinal force determine corrugation formation with necessary initial excitation. It is worth emphasising that in these studies [22–25], the fastening constraints that are identified as the initial excitation to the vehicle–track system play a significant role in corrugation formation. Field observation and tests also indicated that corrugation formation is sensitive to the types of fastenings [11, 26, 27]. Therefore, a systematic investigation of fastening parameters is necessary to better understand and mitigate corrugation.

Fastenings mainly consist of resilient railpads and elastic clamps that together constrain the rail vibrations in three directions. Many fastening models have been developed in the literature, from the relatively simple Kelvin–Voigt (KV) [28] and Poynting–Thomson (PT) models [29] to the more advanced Prony series model [30], fractional derivative model [31, 32], and solid railpad model [33]. With various fastening models, the effects of fastening parameters on vehicle–track dynamic interaction and the resulting defects and rolling noise are analysed. In Ref. [34], the influence of nonlinear railpad parameters on rolling noise was studied, and it was concluded that stiffer railpads can effectively reduce rail-radiated noise. The effect of vertical fastening stiffness on corrugation formation was investigated [35], which indicates that softer railpads can better mitigate corrugation growth. In Ref. [36], the frequency- and temperature-dependent properties of railpads were considered in the high-speed vehicle–track dynamic system, and it is found that the railpad nonlinearity mainly influences the rail vertical accelerations higher than 315 Hz. It was reported that fastening modelling significantly influences the high-frequency vehicle–track interaction at singular rail surface defects, such as squats [37]. Overall, most work mentioned above focuses on studying the effects of vertical fastening constraints on the vehicle–track dynamic interaction. The parametric investigation of longitudinal fastening constraint that determines corrugation initiation [23] has not been performed.

In this paper, we perform a systematic parametric investigation of fastening models employing a 3D FE vehicle–track interaction model, with special attention to the longitudinal fastening constraint. This work is subsequent to the numerical studies on corrugation in Refs. [22, 23] and aims to further understand the corrugation formation mechanism and gain insights into the corrugation mitigation by new fastening design. The structure of this paper is as follows. Section 2 describes the methodology of this paper, including the modelling methods of vehicle–track dynamic interaction, fastenings and wear, and the simulation procedure for corrugation formation. Section 3 analyses the influence of fastening configurations and boundary conditions on corrugation formation. Section 4 studies the effect of fastening parameters (i.e. stiffness and damping) on corrugation formation. Section 5 discusses the effects of train speeds on corrugation features. Section 6 discusses the corrugation formation mechanism under different fastening constraints and some possible corrugation mitigation approaches. Finally, the main conclusions and lines of further research are presented in Sect. 7.

2 Methodology

In this section, the methodology of this work is introduced, including the FE vehicle–track dynamic interaction model, the fastening models with different configurations, boundary conditions and parameters, the wear calculation model, and the simulation procedure for corrugation formation.

2.1 Three-dimensional FE vehicle–track interaction model

2.1.1 Model introduction

Figure 2 shows the 3D transient FE vehicle–track interaction model built with Ansys/LS-DYNA. A Cartesian coordinate system was adopted, where the axes x, y, and z are in the longitudinal (rolling), lateral, and vertical directions, respectively. The model considered a straight track and a half-track, and a half wheelset was included for computation efficiency. It should be noted that this assumption does not necessarily mean the identical conditions for the right and left half wheelset–track systems. They could have different parameters (i.e. fastening constraints), leading to different characteristics of wheel–rail dynamic interaction and corrugation. The structures above the primary suspension of the vehicle were simplified as mass elements as their vibration frequency is usually not high than 10 Hz [38]. The wheel has a nominal radius of 0.46 m with a conicity of 1/40. The rail profile is UIC 54E1 with 1/40 inclination. The wheelset, rail, and sleeper were all modelled with 3D solid elements according to their nominal geometry and material properties, as listed in Table 1. The solution zone with a meshing size of 0.8 mm starts at 0.3 m from the initial wheel location (position O in Fig. 2, corresponding to 0 m). The mesh sensitivity analysis in Ref. [39] indicates that a meshing size of 0.8 mm is acceptably accurate for the engineering calculation. The inner end of the wheel axle is constrained in the lateral direction to keep the rolling wheel from toppling over. The two ends of the rail are constrained in the lateral and longitudinal directions with non-reflective boundary conditions to reduce the numerical errors from the finite length rail [40]. The sleeper was connected to the rail through the fastenings and supported by the ballast. The primary suspension and the ballast were modelled as multiple spring–damper elements. Several fastening models corresponding to different service stages of fastenings in the field track were built up and applied to the whole track, as described in detail in Sect. 2.2. The track length is 20.54 m, including 34 sleeper spans. The total number of elements is 1,135,388, and the total number of nodes is 1,297,900. The parameters of the vehicle–track system are listed in Table 1, which are commonly used to study the Dutch railway system [14, 22].

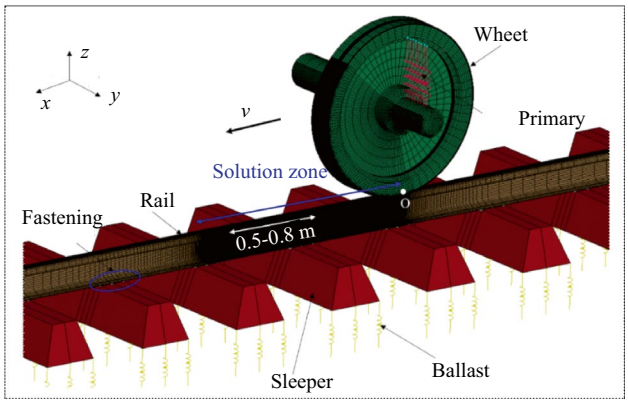

Fig. 2 Three-dimensional FE vehicle–track dynamic interaction model

The contact between the wheel and rail was modelled with a surface-to-surface contact algorithm based on a penalty approach [41], allowing the wheel either contacts or separate from the rail [40]. The mechanical contact filtering effect is inherently included in the numerical calculations. Coulomb's frictional law was applied with a friction coefficient of 0.4. The traction coefficient is 0.15. The angle of attack is set to be approximately zero to simulate the small wheel–rail lateral interaction on straight tracks. An implicit–explicit sequential approach was employed in the simulation to minimise the solution time and the dynamic effects during the initialisation of the wheel–rail interaction.

Table 1 Vehicle and track parameters [14, 22]

Parameters		Values	Parameters		Values
Sprung mass		7200 kg	Wheel and rail material	Young's modulus	210 GPa
Primary suspension	Vertical stiffness	1.15 MN/m		Poisson's ratio	0.3
	Vertical damping	2.5 kNs/m		Density	7800 kg/m^3
Railpad	Vertical stiffness	1300 MN/m	Sleeper material	Young's modulus	38.4 GPa
	Vertical damping	45 kNs/m		Poisson's ratio	0.2
Ballast	Vertical stiffness	45 MN/m		Mass density	2520 kg/m^3
	Vertical damping	32 kNs/m		Spacing (L)	0.6 m

In the implicit calculation, the vehicle–track system reached an equilibrium state under gravity. The calculated nodal displacement was subsequently input as an initial condition of the explicit calculation of the vehicle–track dynamic interaction. In the explicit calculation, initial forward translation and rotation velocities were prescribed to the wheel model to generate rolling motion. The same initial translation velocity was applied to the car body and bogie. The time step for the explicit mechanical solver was 4.67×10^{-8} s, which is small enough to meet the Courant stability condition. A rolling distance of 0.3 m from the wheel initial position to the solution zone was applied for the dynamic relaxation [40], which is sufficiently long to damp the oscillations caused by the wheel/rail initial kinematic and potential energy [39, 40]. The model simulates a Dutch passenger vehicle with a speed of 140 km/h. The wheel and rail surfaces are smooth at the beginning before corrugation initiation. The rail corrugation will be applied to the model by adjusting the corresponding rail nodal coordinates in the input files [40].

2.1.2 The validity of the FE model

This vehicle–track interaction model has been extensively validated in terms of frictional rolling contact solutions [39], wheel dynamics [42], and track dynamics [43, 44]. The model also explained the formation process of rail squats and was validated by extensive field monitoring [45, 46]. In terms of corrugation studies, this model has been first used in Ref. [22], and it is found that the corrugation could not grow but was erased by the wheel–rail interaction because a model of nominal fastenings is used. Afterwards, this model was used in Ref. [23], and it successfully reproduced the consistent initiation and growth of corrugation by using a model of degraded fastenings that allow flexibility for rail longitudinal vibration. The reproduced corrugation agrees with the field corrugation in terms of spatial distribution and major wavelength components. The identified corrugation formation mechanism has been verified in the laboratory tests using the V-Track test rig. The work in Refs. [22, 23] has highlighted the significance of fastening longitudinal constraints on corrugation development. This paper is subsequent to them and employs this model to perform a comprehensively parametric investigation of fastenings to better understand the corrugation formation mechanism and gain insights into corrugation mitigation by the fastening design.

2.2 Fastening models

The railway fastenings, mainly consisting of railpads and clamps, are used to constrain the rail to the sleepers in the vertical, longitudinal, and lateral directions and filter out the high-frequency vibrations from the rail [36, 47]. Due to the dynamic train loads during long-term service, fastenings become gradually degraded. Figure 3 shows four examples of fastening degradation observed on the Dutch railway. The fastening bolt may loosen, and the railpad might be displaced, as shown in Fig. 3a and b. Due to the irregular wear, railpads may lose their original geometry (see Fig. 3c and d), and the rail may not necessarily be in uniform contact with the railpads and hence not be uniformly constrained. Different configurations of fastenings with various boundary conditions and parameters are designed (see Table 2) to consider these constraining conditions and analyse their influences on corrugation formation.

2.2.1 Fastening models with different configurations

Figure 4a shows a fastening model applied in the FE vehicle–track interaction model, designated as RPM1. In the vertical direction, the fastening was represented by 3×4 linear spring–damper elements (i.e. three columns in the longitudinal dimension and four rows in the lateral) to realistically simulate the area support between the rail and sleeper and achieve a balance between the simulation accuracy and computation efficiency [43]. The fastening elements connect the rail bottom nodes (marked by R) and sleeper nodes (marked by S). Each of the 12 elements has the same parameters, equal to 1/12 of the nominal values, which are obtained by fitting the simulated track dynamics to the field hammer tests [43]. The longitudinal and lateral restrictions of the fastening were considered as rigid constraints to the rail and sleeper nodes. Although this is a simplification of the nominal track situation, it has been proven to be appropriate for representing track dynamics [43] and wheel–rail

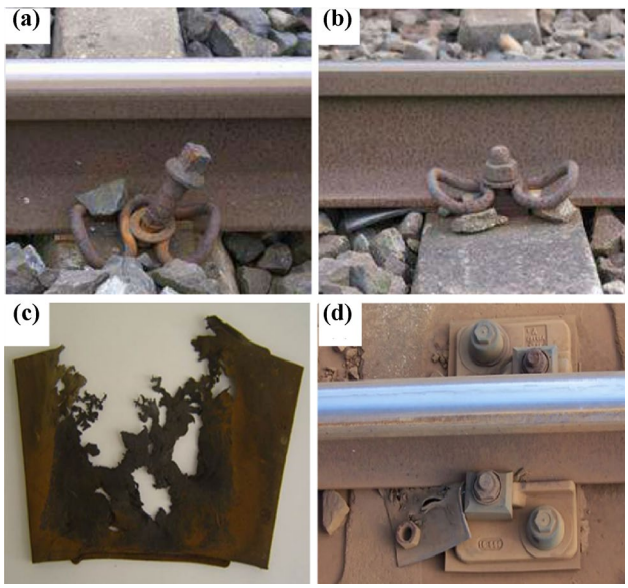

Fig. 3 Fastening degradation from Dutch railway: **a** loose fastening bolt; **b** displaced railpad; **c** worn railpad 1; **d** worn railpad 2

Table 2 Variation of fastening models

Fastening model (RPM)	Description	Purposes
1	Configuration: 3×4 Vertical: spring–damper pairs Longitudinal: rigid constraint Lateral: rigid constraint	To model a nominal track situation (corresponding to Fig. 4a)
2	1×4 in the 2nd column	To investigate the influence of fastening configurations on corrugation formation (corresponding to Fig. 4b)
3	2×4 in the 1st and 3rd columns	
4	3×2 in the 2nd and 3rd rows (inner)	
5	3×2 in the 1st and 4th rows (outer)	
6	Releases the longitudinal fastening constraint of RPM1 in the 1st and 3rd columns	To investigate the influence of fastening boundary conditions on corrugation formation (corresponding to Fig. 5)
7	Releases the longitudinal fastening constraint of RPM1 in the 2nd column	
8	Releases the outer longitudinal fastening constraint of RPM1 in the 1st and 4th rows	
9	Releases the inner longitudinal fastening constraint of RPM1 in the 2nd and 3rd rows	
10	Longitudinal springs with stiffness of 150 MN/m	Configuration: 3×4; Vertical and lateral: the same as RPM1
11	Longitudinal springs with stiffness of 300 MN/m	To investigate the influence of fastening longitudinal stiffness on corrugation formation (corresponding to Fig. 6)
12	Longitudinal springs with stiffness of 900 MN/m	
13	Add longitudinal damping of 6 kNs/m to RPM11	To investigate the influence of fastening longitudinal damping on corrugation formation
14	Add longitudinal damping of 24 kNs/m to RPM11	

dynamic interaction [42, 48]. The schematic drawing of RPM1 is shown in Fig. 4b. The red and yellow triangles represent rigid constraints to the rail nodes from fastenings in the longitudinal and lateral directions, respectively. To consider non-uniform constraints of fastenings due to, i.e. railpad degradation, other four types of configurations are designed, 1×4 in the 2nd column (RPM2), 2×4 in the 1st and 3rd columns (RPM3), 3×2 in the 2nd and 3rd rows (RPM4), and 3×2 in the 1st and 4th rows (RPM5), respectively, as shown in Fig. 4b. RPM4 constrains the inner rail nodes under the rail web along the lateral dimension while RPM5 the outer.

2.2.2 Fastening models with different boundary conditions

It is reported [22, 23] that differential wear that causes initial corrugation is dominated by rail longitudinal compression modes and sensitive to the longitudinal boundary conditions of fastenings. Therefore, in this paper, the longitudinal boundary conditions of fastenings are varied to investigate their influences on corrugation formation and also attempt to gain insight into corrugation mitigation. Figure 5 shows schematic drawings of four fastening models with different boundary conditions, RPM6–RPM9. Compared to RPM1, RPM6 and RPM7 vary the column number of the fastening longitudinal boundary conditions in the longitudinal dimension, while RPM8 and RPM9 vary the row number in the lateral dimension. Specifically, RPM6 releases the fastening longitudinal constraint of RPM1 in the 1st and 3rd columns, while RPM7 is in the second column. RPM8 keeps the fastening longitudinal constraint of RPM1 in the 2nd and 3rd rows (inner), while RPM9 in the 1st and 4th rows (outer). The lateral boundary conditions of RPM6–RPM9 are the same as those of RPM1.

2.2.3 Fastening models considering longitudinal stiffness and damping

The fastening models defined in Sect. 2.2.2 simplified the fastening longitudinal restriction as rigid constraints to the rail nodes. In reality, the rail has certain flexibility on the elasticity of railpads in the longitudinal direction, similar to that in the vertical direction. Therefore, a more realistic representation of fastening longitudinal constraint should consider the longitudinal stiffness and damping by, such as multiple spring–damper elements, as shown in Fig. 6.

Unlike the vertical ones, the fastening longitudinal parameters have been barely reported in the literature. Zhang et al. [49, 50] studied the 3D rail vibrations under fastening constraints and calibrated 3D fastening parameters with ZW692 railpads by best fitting to the hammer test measurements. The derived longitudinal stiffness and damping of fastenings are around 160 MN/m and 6 kNs/m, respectively. Oregui et al. [30] compared the master curves of new and worn railpads and found that the damping behaviour of the worn railpads is nearly non-existent and thereby

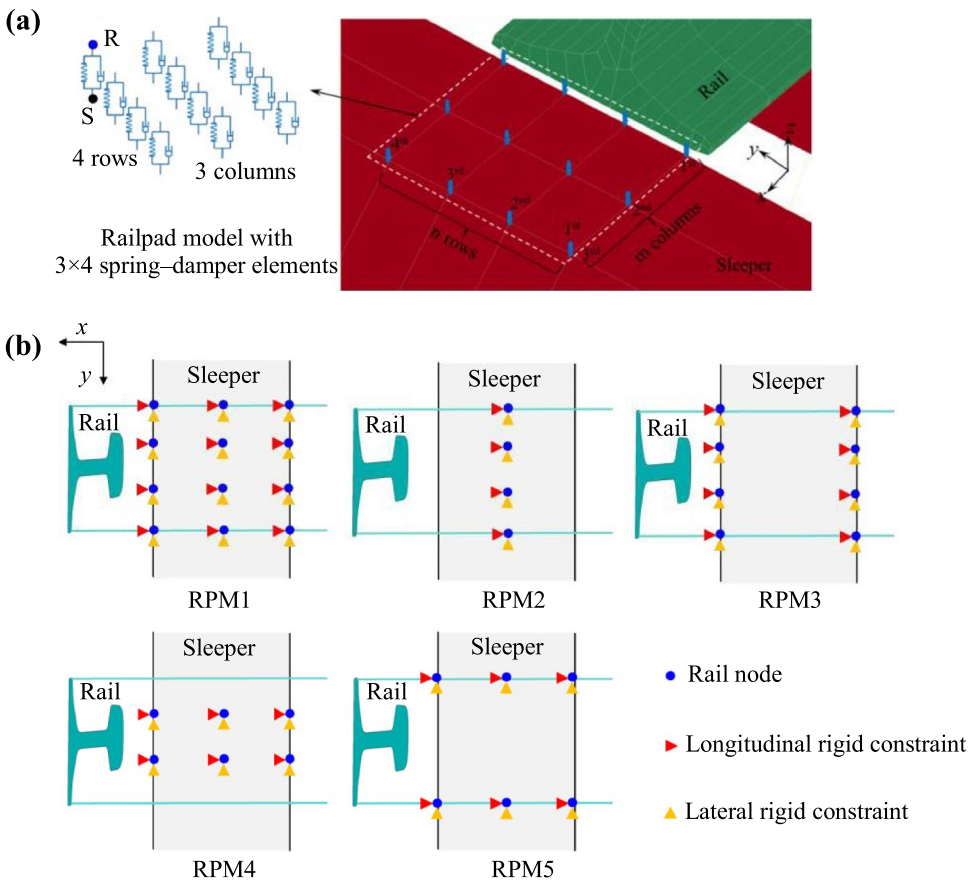

Fig. 4 Fastening models with different configurations: **a** fastening model RPM1 in the FE vehicle–track interaction model; **b** schematic drawings of fastening models RPM1–RPM5 with different configurations

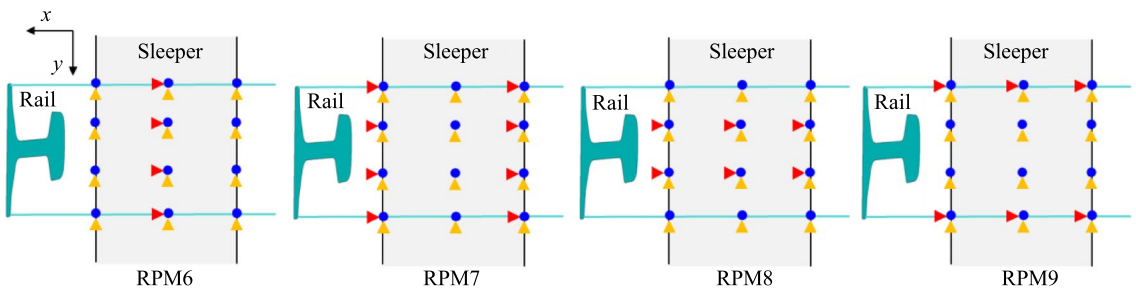

Fig. 5 Schematic drawings of fastening models RPM6–RPM9 with different longitudinal boundary conditions

becomes purely elastic. Besides, the stiffness of fastenings may significantly reduce due to the looseness and railpad ageing [30]. Considering different types of railpads and the ageing effect, five fastening models with different longitudinal stiffness and damping values are designed. RPM10–12 modelled fastenings by 3 × 4 spring elements with the stiffness values of 150, 300, and 900 MN/m, respectively. Damping is not considered in these three models to simulate the severely worn railapds. RPM13–14 simulated fastenings by 3 × 4 spring–damper pairs with the damping of 6 kNs/m and 24 kNs/m, respectively. The stiffness of these two models is 300 MN/m, the same as RPM11.

2.3 Wear model

The wear of the rail surface is assumed to be proportional to the accumulated frictional work during wheel passages

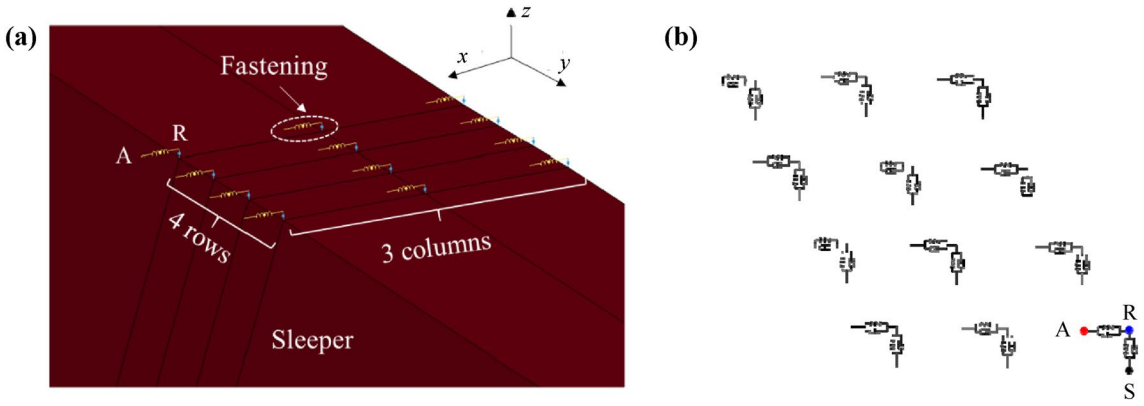

Fig. 6 The fastening model considering longitudinal stiffness and damping: **a** fastening model in the FE vehicle–track interaction model; **b** schematic drawings of the fastening model. R refers to rail nodes, S refers to sleeper nodes, and A refers to end nodes of the longitudinal spring–damper pairs

[5, 51]. In the FE simulation, the frictional work at each node is calculated for a wheel passage, i.e. from the node entering until leaving the contact patch as follows:

$$w(x,y) = kW_{\mathrm{f}}(x,y) = k\sum_{i=1}^{N}\tau_i(x,y)v_i(x,y)\Delta t, \tag{1}$$

where k is the wear coefficient, W_{f} (x, y) is the frictional work, τ_i (x, y) and v_i (x, y) are the local tangential stress and micro-slip, respectively, and N is the number of time steps Δt during which a node passes the contact patch. The tangential stress is calculated by the nodal force divided by the corresponding area in the FE model, and the micro-slip is calculated as the relative nodal velocity between two contacting wheel and rail nodes. The more detailed calculation method of the tangential stress and micro-slip can be found in [40].

2.4 Simulation procedure for corrugation formation with different fastening models

The simulation procedure for corrugation formation includes four steps [23], as shown in Fig. 7a.

In step 1, one of the fastening models from Table 1 is applied in the 3D FE vehicle–track interaction model. The rail is smooth in the beginning, i.e. without corrugation. Let the wheel roll over the track and calculate the differential wear after the first wheel passage.

In step 2, if this wear has a negligibly small fluctuation amplitude (e.g. ≤ 0.8 in Fig. 8a), corrugation will not develop with the current fastening model, which will then be dropped. Otherwise, it means that this fastening model can serve as the initial excitation to the vehicle–track system. Rail longitudinal compression modes are excited, causing dynamic longitudinal contact force and initial differential wear. This differential wear will result in the very initial corrugation whose severity is quantified with a maximal peak to trough distance $(2A_{\mathrm{max}})_0$. The examples of initial differential wear can be seen in the top figure of Fig. 7b.

In step 3, the obtained initial corrugation of $(2A_{\mathrm{max}})_0$ is applied to the rail surface after scaling by adjusting the nodal coordinates in the input files of the dynamic analysis solver. This scaling is to account for the multiple wheel passages that contribute to consistent corrugation growth. It is proportional to and in anti-phase with the initial differential wear (see an example in the bottom figure of Fig. 7b). Anti-phase means a wear peak causes a corrugation trough. Similarly, additional wear from step 4 is added to the corrugation in the subsequent wheel passages. The rail is thus with corrugation, which can be in its initial form of $(2A_{\mathrm{max}})_0$ as from step 1 or in a more advanced form of $(2A_{\mathrm{max}})_i$ $(i = 1, 2, 3, \ldots)$ as from step 4. The corrugation is an additional excitation besides the initial excitation. Both excitations can cause differential wear of their respective wavelengths.

In step 4, let the wheel roll over the corrugated rail, and calculate the differential wear caused by the joint excitation from the fastening model and the corrugation. Subsequently, check if the consistency condition is satisfied, i.e. if the differential wear is in phase with the initial differential wear and in anti-phase with the existing corrugation. If the condition is satisfied, it means that corrugation can continuously grow, and then repeat steps 2, 3, and 4 with increased $(2A_{\mathrm{max}})_i$ until a limiting amplitude $(2A_{\mathrm{max}})_{\mathrm{l}}$, with which the condition is not satisfied anymore. When the condition is not satisfied, the simulation will stop, and another fastening model will be analysed, repeating steps 1–4.

Figure 7b shows an example of the corrugation initiation and consistent growth with RPM6 to better illustrate the simulation procedure. Five trial corrugation amplitudes $(2A_{\mathrm{max}})_i$ $(i = 0, 1, \ldots, 4)$ of 0, 10, 40, 80, and 160 μm were applied

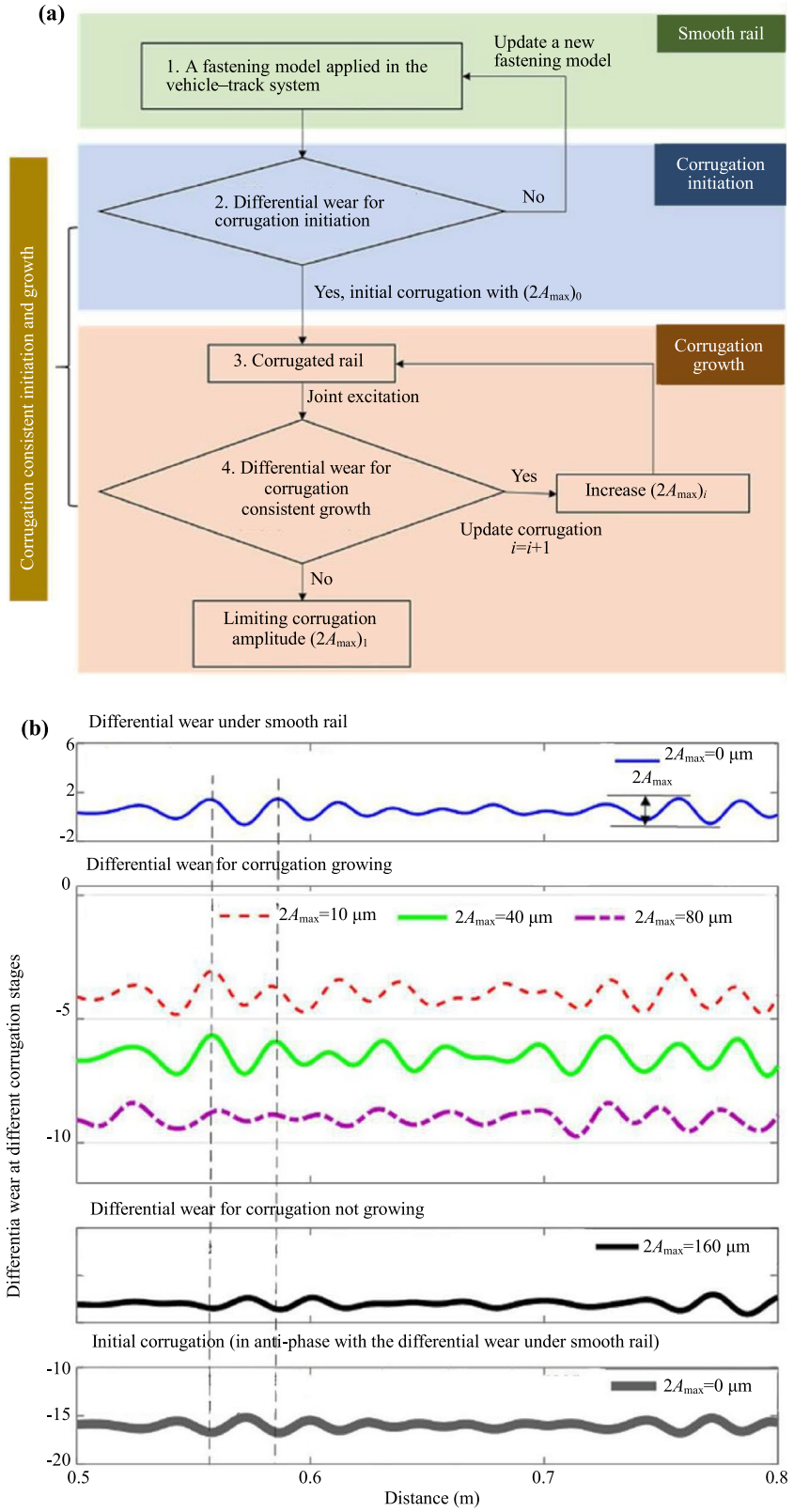

Fig. 7 The simulation procedure for corrugation formation with different fastening models [23]: **a** the flowchart of the simulation procedure and **b** an example of corrugation initiation and consistent growth with RPM6

in the simulation, which are scaled to the initial differential wear and have the same spatial distribution. More details about the simulation procedure can be found in Ref. [23].

3 The influence of fastening configurations and boundary conditions on corrugation formation

In this section, the influence of fastening configurations and boundary conditions on corrugation formation is analysed based on the numerical simulation results.

3.1 Fastening configurations

Figure 8 shows the spatial distributions of differential wear under increasing trial corrugation amplitude (10, 40, and 160 μm) with two fastening configurations RPM1 and RPM2. In reality, forming a corrugation with a certain amplitude requires many wheel passages. But here, we assume that the corrugation will consistently grow till $(2A_{\max})_i$ and thus simplify this process by scaling the initial differential wear amplitude to a 'trial' amplitude, corresponding to different corrugation growth stages. The fluctuation amplitude of the initial differential wear with RPM2 is considerably larger than that with RPM1 and with different spatial distributions, causing different initial corrugations as shown in Fig. 8. With RPM 1, after applying corrugation amplitude $2A_{\max}=10$ μm, the differential wear due to the joint excitations of the initial excitation and the corrugation tends to vary from initial differential wear and the consistency condition for corrugation growth can barely hold. When further increasing the corrugation amplitude up to $2A_{\max}=40$ μm, the differential wear tends to be in anti-phase with the initial differential wear and in-phase with the existing corrugation, as shown in Fig. 8a. In this case, the existing corrugation will be levelled out. In contrast, with RPM 2, the consistency condition between differential wear and corrugation is still satisfied when amplitude $2A_{\max}=40$ μm, as shown in Fig. 8b, indicating that corrugation can at least continuously grow up to 40 μm. With a relatively large trial amplitude $2A_{\max}=160$ μm, the differential wear becomes anti-phase with the initial differential wear, and the existing corrugation will be erased, indicating that the corrugation with RPM2 cannot infinitely grow, e.g. limiting $2A_{\max}$ not exceeding 160 μm. There should be an intermediate stage of corrugation amplitude, limiting amplitude in Fig. 7, between 40 and 160 μm, in which the corrugation formation reaches a saturation state without further accumulation of differential wear.

Overall, with fastening configuration RPM1, corrugation can barely grow up to 10 μm, while with RPM2, it can at least grow up to 40 μm. Compared to RPM2 (1×4 configuration), RPM1 (3×4 configuration) provides a much stronger longitudinal constraint to the rail, as shown in Fig. 4b. Hence, rail longitudinal compression modes with RPM1 are more

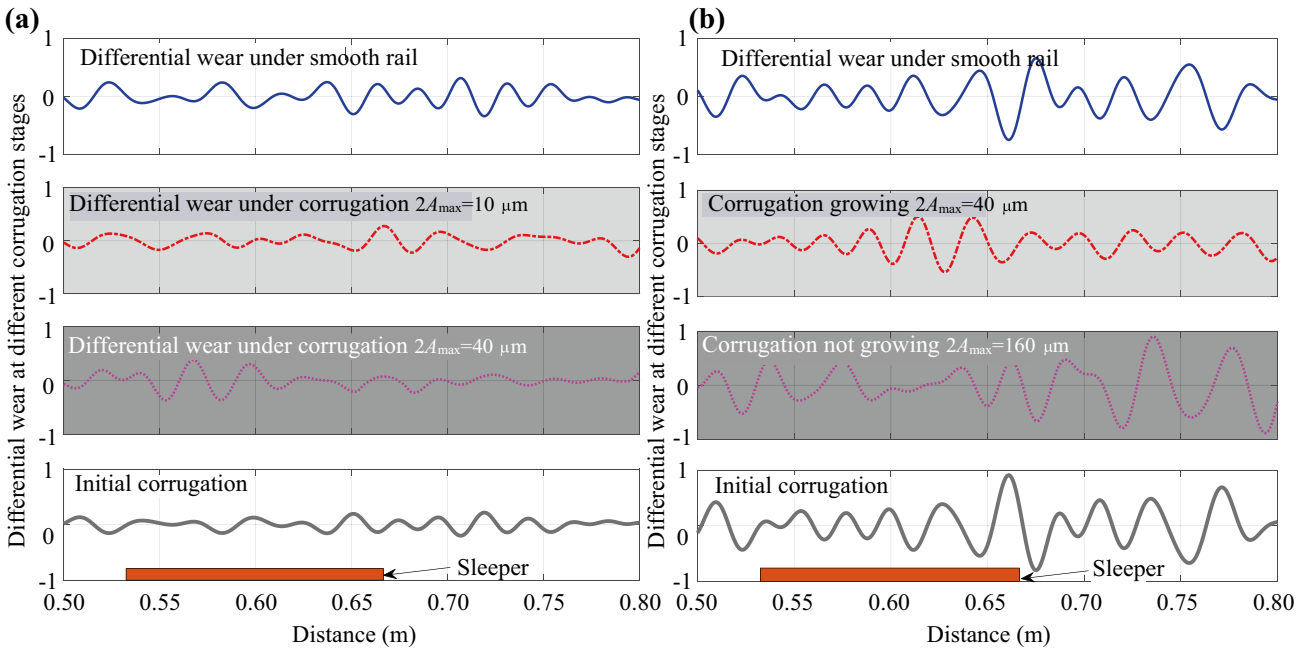

Fig. 8 Differential wear in the spatial domain with fastening configurations RPM1 and RPM2: **a** differential wear at different corrugation stages with RPM1 and **b** differential wear at different corrugation stages with RPM2. The sleeper position starts from 0.53 m and ends at 0.67 m, as shown in this figure. It keeps the same for the figures below

severely suppressed, leading to considerably smaller fluctuation amplitudes of the dynamic longitudinal contact forces and the resulting initial differential wear. From these two cases, we can conclude that the limiting corrugation amplitude is dependent on the intensity of the initial excitation determined by the fastening model, and the resulting dynamic longitudinal contact force and initial differential wear. Higher fluctuation amplitude of initial differential wear tends to grow into severer corrugation with larger limiting amplitude. Initial differential wear rate can hence be considered as an indicator of the possible severity of the maximum mature corrugation. In addition, according to the consistency condition, corrugation has the same features as initial differential wear in terms of spatial distribution and major wavelength components. Therefore, we mainly analyse the influence of fastening models on initial differential wear hereinafter.

Figure 9 shows the features of initial differential wear under the various fastening configurations of RPM1–RPM5. Comparing the results of RPM1–RPM3 in Fig. 9a and c, it is found that the variation of column number of fastening constraints significantly influences the spatial distribution and wavelength components of initial differential wear. Specifically, the result of the RPM1 model shows the lowest level of initial differential wear. In the latter two configurations, i.e. RPM 2 and RPM 3, initial differential wear has relatively larger fluctuation amplitudes and contains major wavelength components between 20 and 50 mm (corresponding to about 800–2000 Hz with a speed of 140 km/h). One difference between the two latter configurations is that there are three major wavelength components at 22.0, 28.6, and 37.7 mm with RPM2, while there contains only one major wavelength component at 25.6 mm with RPM3. Besides, the fluctuation amplitude of initial differential wear with RPM2 is larger than that with RPM3. That is because RPM3 (2×4 configuration) provides a stronger fastening constraint to the rail than RPM2 (1×4 configuration), and thus, longitudinal compression modes are suppressed more with reduced vibration amplitudes.

Comparing the results of RPM4 (3×2 configuration, inner, see Fig. 4b) and RPM1 (3×4 configuration) in Fig. 9b and d, it is found that initial differential wear with RPM4 has a low level similar to that of RPM1. In comparison with RPM1,

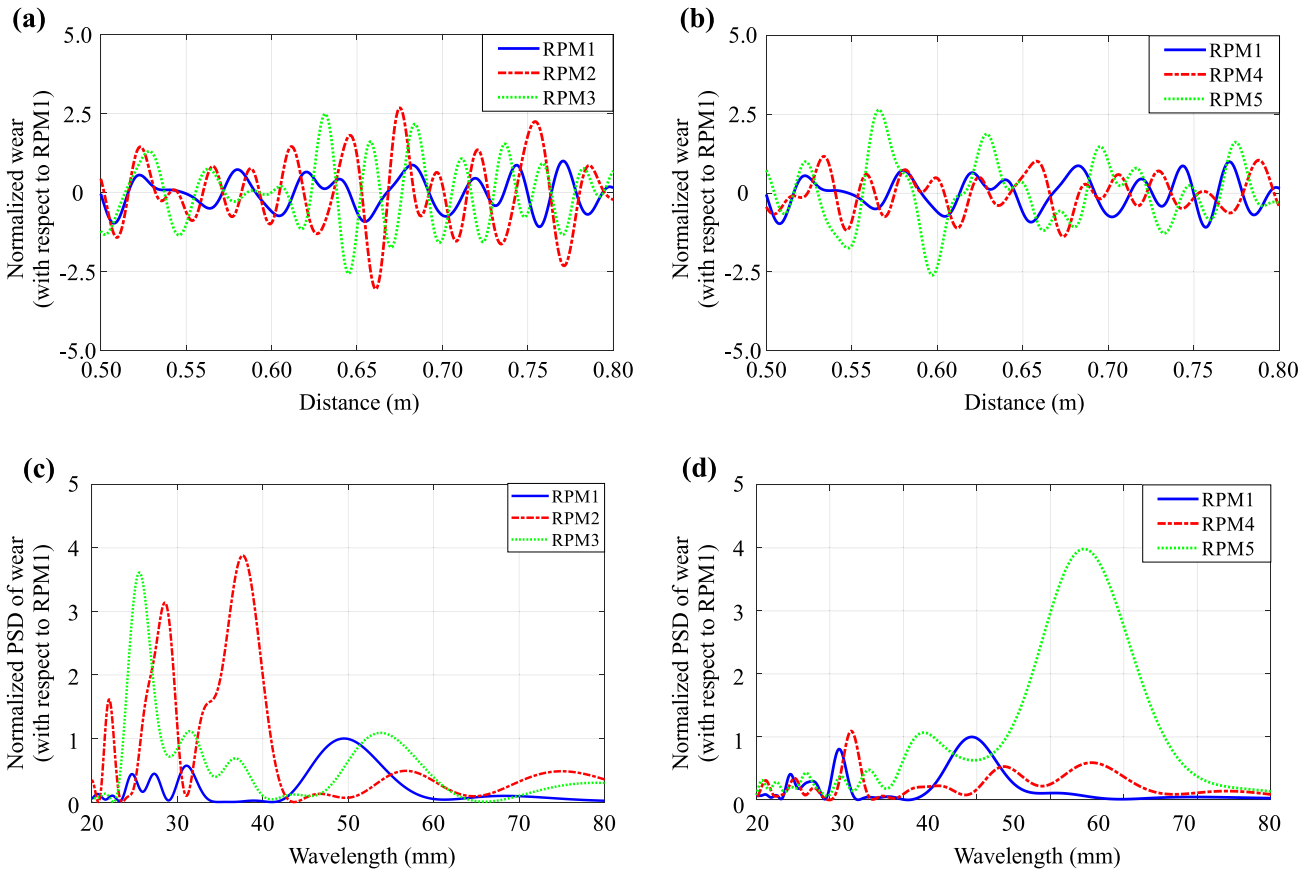

Fig. 9 Initial differential wear at the first wheel passage in spatial and wavelength domains with different fastening configurations RPM1–RMP5: **a** initial differential wear in the spatial domain under RPM1–RPM3; **b** initial differential wear in the spatial domain under RPM1, RPM4, and RPM5; **c** initial differential wear in the wavelength domain under RPM1–RPM3; and **d** initial differential wear in the wavelength domain under RPM1, RPM4, and RPM5

RPM4 removes the fastening constraints in the 1st and 4th rows. Corrugation can barely grow in this condition, as shown in Fig. 8a. This result indicates that the inner fastening constraints in the 2nd and 3rd rows can effectively suppress rail longitudinal compression modes and mitigate corrugation. When we removed the fastening constraints of RPM1 in the 2nd and 3rd rows (corresponding to RPM5, 3×2 configuration, outer, see Fig. 4b), a dominant wavelength component at about 64.7 mm (about 600 Hz with a speed of 140 km/h) with larger fluctuation amplitude is observed in Fig. 9b and d. The fluctuation amplitude of wavelength components between 20 and 50 mm remains small. These results indicate that the outer fastening constraints in the 1st and 4th rows can only mitigate corrugation with relatively shorter wavelengths (i.e. 20–50 mm), while the relatively longer-wavelength corrugation (i.e. 64.7 mm) can still develop.

In summary, fastening configurations significantly influence the spatial distribution and wavelength components of corrugation. Specifically, initial differential wear and corrugation are sensitive to the fastening configurations in the longitudinal dimension, i.e. the column number of spring–damper elements. When increasing the column number from one (RPM2) to two (RPM3), the major wavelength components of initial differential wear decrease from three to one, and the fluctuation amplitude also reduces. When further increasing the column number to three (RPM1), initial differential wear has the lowest level and corrugation barely grows. These results point out a direction for corrugation mitigation by increasing the column number or the fastening constraints in the longitudinal dimension. With the same column number as RPM1, it is shown that variation of row number (RPM4 and RPM5) can effectively change the wavelength of the main corrugation components. Specifically, the removal of inner fastening constraints in the 2nd and 3rd rows (RPM5) leads to the formation of a relatively longer-wavelength corrugation. Therefore, for corrugation mitigation, inner fastening constraints in the 2nd and 3rd rows are necessary.

3.2 Fastening longitudinal boundary conditions

Figure 10 shows the features of initial differential wear with fastening models under different longitudinal boundary conditions (RPM1 and RPM6–RPM9, see Fig. 5). Comparing the results of RPM1, RPM6, and RPM7 in Fig. 10a and c, it is found that the variation of number of columns of longitudinal rigid constraints considerably affects the spatial distribution and wavelength components of initial differential wear. Specifically, initial differential wear with RPM6 has the highest power intensity with four major wavelength components. Corrugation can consistently initiate and grow up to 80 μm in this condition [23]. Compared to that of RPM6, the fluctuation amplitude of initial differential wear with RPM7 is smaller, and the number of major wavelength components decreases from four to two, which is caused by the relatively stronger longitudinal constraints to the rail, as shown in Fig. 5. Initial differential wear with RPM1 has the lowest fluctuation level, and corrugation can barely grow.

Comparing the results of RPM1, RPM8, and RPM9 in Fig. 10b, it can be seen that the variation of number of rows of longitudinal rigid constraints has little influence on the spatial distribution and fluctuation amplitude of initial differential wear. However, Fig. 10d shows that the PSD magnitude at 48.6 mm with RPM9, which releases the longitudinal rigid constraint of RPM1 in the 2nd and 3rd rows, increases to about twice those with RPM1 and RPM8. Initial differential wear with RPM5, which has the same longitudinal fastening constraint as RPM9, also shows a dominant peak at 64.7 mm. These results indicate that the absence of inner longitudinal constraint in the 2nd and 3rd rows seems a preferred condition for the formation of relatively longer-wavelength corrugation. Meanwhile, it should be noted that the initial differential wear of RPM5 and RPM9 is different from each other, indicating that fastening vertical and lateral constraints also influence the rail longitudinal compression modes and the corrugation features.

In summary, initial differential wear and corrugation are sensitive to the number of columns of fastening longitudinal boundary conditions. When gradually reducing the column number from three (RPM1) to two (RPM7) and further to one (RPM6), the fluctuation amplitude of initial differential wear significantly increases, as well as the number of major wavelength components. This result, in turn, suggests that the increase in column number, or rail constraint in the longitudinal dimension contributes to corrugation mitigation. With the same number of columns as RPM1, initial differential wear and corrugation seem insensitive to the variation of the number of rows of the fastening longitudinal boundary conditions (RPM8 and RPM9), except for a relatively longer-wavelength corrugation at 48.6 mm. Further, a common feature is found between the fastening longitudinal boundary conditions and the fastening configurations that corrugation is more sensitive to the variation of column number (in the longitudinal dimension) than the row number (in the lateral dimension). That is because the rail longitudinal modes, which are responsible for corrugation initiation, are a type of compression/rarefaction vibration in the longitudinal direction. This result also indicates that the fastening longitudinal constraint to the rail is the major factor that determines the corrugation formation.

4 Influence of fastening longitudinal stiffness and damping

Figure 11 shows the spatial distribution of differential wear under different corrugation severities with RPM10 (see Fig. 6). The longitudinal fastening stiffness of RPM10 is

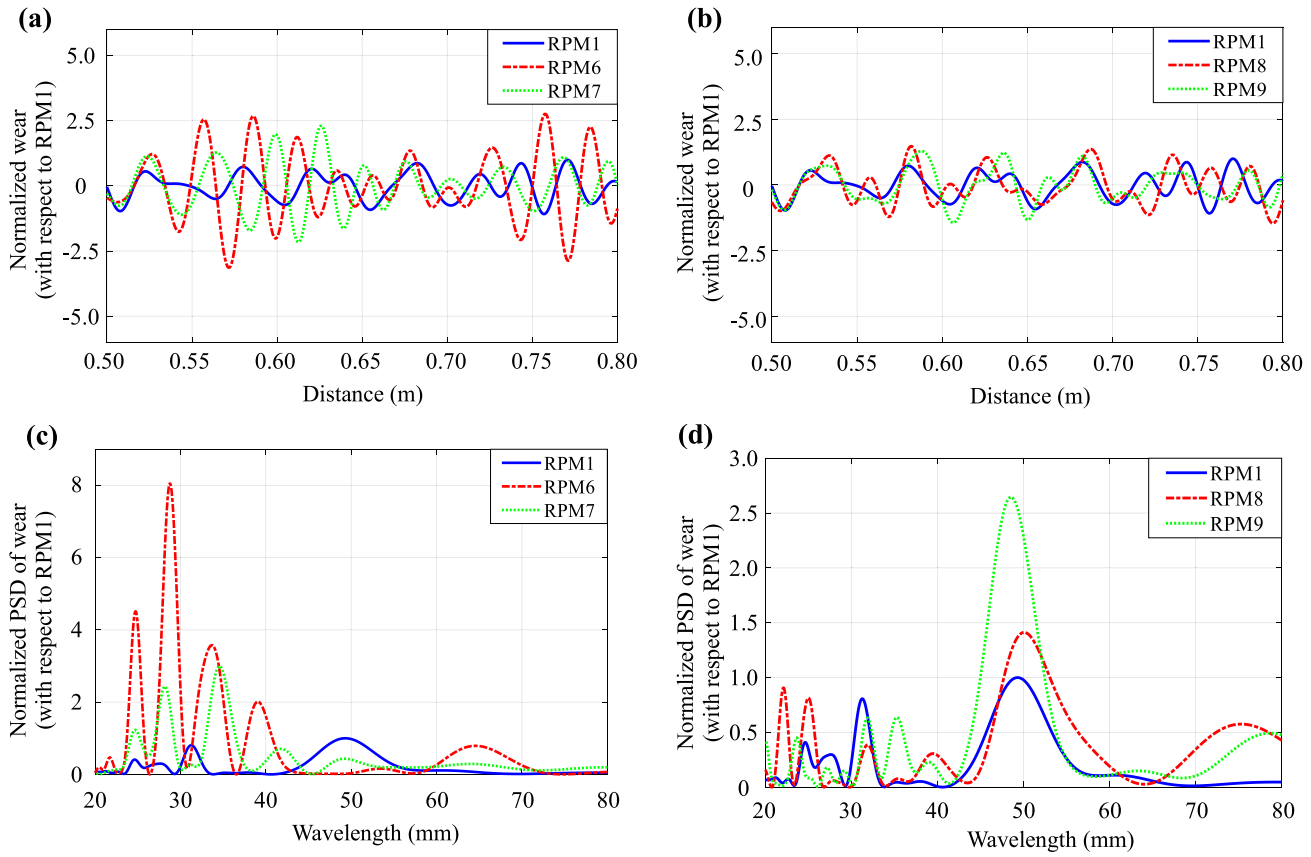

Fig. 10 Initial differential wear in spatial and wavelength domains with different fastening boundary conditions RPM1 and RPM6–RMP9: **a** initial differential wear in the spatial domain under RPM1, RPM6, and RPM7; **b** initial differential wear in the spatial domain under RPM1, RPM8, and RPM9; **c** initial differential wear in the wavelength domain under RPM1, RPM6, and RPM7; **d** initial differential wear in the wavelength domain under RPM1, RPM8, and RPM9

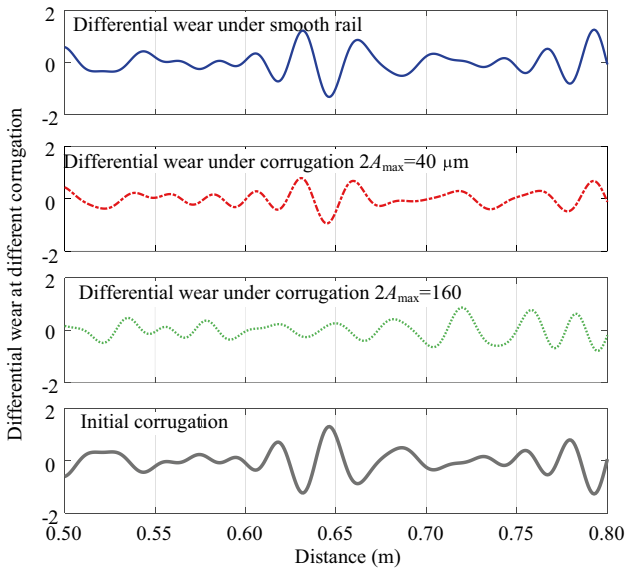

Fig. 11 Differential wear in the spatial domain with RPM10

150 MN/m, and the longitudinal fastening damping is not considered to simulate severely worn railpads without damping capacity [30]. It can be seen that when amplitude $2A_{max} = 40$ μm, differential wear is in-phase with the initial differential wear and anti-phase with corrugation, indicating that corrugation can consistently grow up to 40 μm with RPM10. This result also suggests that the introduction of the fastening longitudinal stiffness is capable of reproducing consistent corrugation initiation and growth. The consistency condition that the differential wear is in anti-phase with the corrugation is not satisfied with a trial amplitude $2A_{max} = 160$ μm, indicating that the limiting corrugation amplitude is below 160 μm with RPM10. In the following sections, we will further vary fastening longitudinal parameters (i.e. stiffness and damping) and analyse their effects on corrugation formation.

4.1 Influence of fastening longitudinal stiffness

Figure 12 shows the spatial distribution and wavelength components of initial differential wear with different

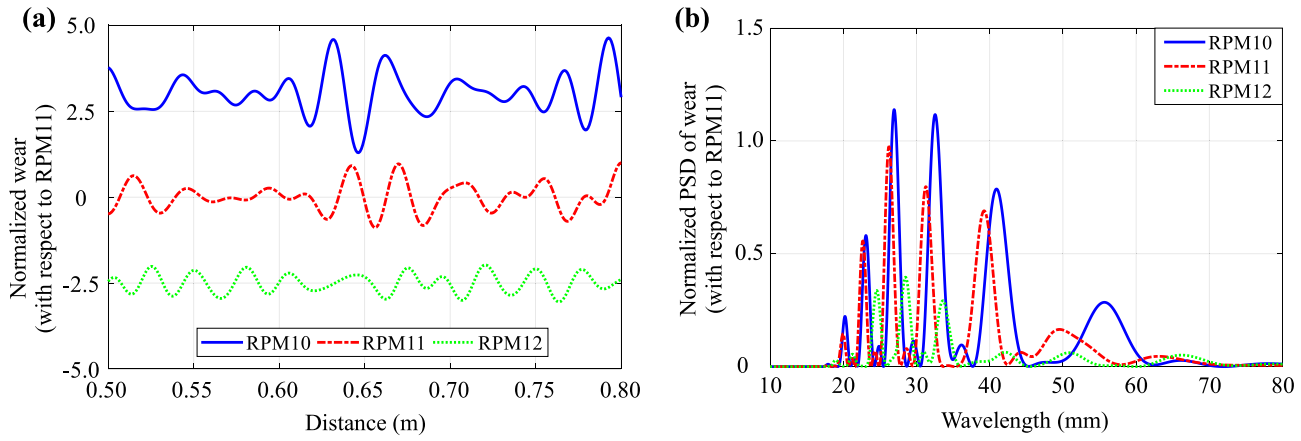

Fig. 12 Initial differential wear in spatial and wavelength domains with different fastening longitudinal stiffness: **a** initial differential wear in the spatial domain under RPM10, RPM11, and RPM12 and **b** initial differential wear in the wavelength domain under RPM10, RPM11, and RPM12

fastening longitudinal stiffness of 150 MN/m (RPM10), 300 MN/m (RPM11), and 900 MN/m (RPM12), as listed in Table 2. The fastening longitudinal damping is not considered. When the stiffness is small (RPM10), initial differential wear shows a larger fluctuation amplitude but the wave patterns with high amplitude mainly occur in the local positions between 0.6 and 0.7 m and after 0.75 m, as shown in Fig. 12a. With the increase in longitudinal stiffness (RPM11 and RPM12), the fluctuation amplitudes of initial differential wear decrease but the wave patterns become more continuously and evenly distributed along the rail between 0.5 and 0.8 m. Figure 12b shows initial differential wear in the wavelength domain. It can be seen that the increase in fastening longitudinal stiffness shifts the major wavelength components to the shorter ones with significantly reduced magnitude. That is because that larger longitudinal stiffness increases the frequencies of longitudinal compression modes and reduces the corresponding vibration amplitudes [50]. These results indicate that increasing fastening longitudinal stiffness is helpful to mitigate corrugation.

4.2 Influence of fastening longitudinal damping

Figure 13 shows the spatial distribution and wavelength components of initial differential wear with different fastening longitudinal damping of 0 kNs/m (RPM11), 6 kNs/m (RPM13), and 24 kNs/m (RPM14), as listed in Table 2. The fastening longitudinal stiffness in these three cases is 300 MN/m. When damping increases from 0 to 6 kNs/m, the fluctuation amplitude of initial differential wear is significantly attenuated while the major wavelength components do not change. That is because larger longitudinal damping leads to smaller fluctuation amplitude of longitudinal compression modes without frequency shifts [50]. When further

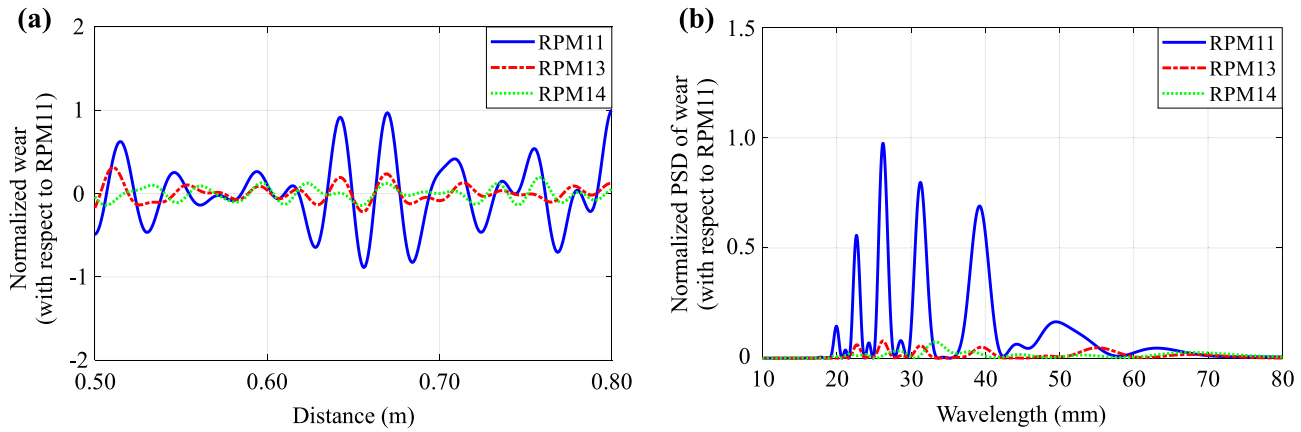

Fig. 13 Initial differential wear in spatial and wavelength domains with different fastening longitudinal damping: **a** initial differential wear in the spatial domain under RPM11, RPM13, and RPM14; **b** initial differential wear in the spatial domain under RPM11, RPM13, and RPM14

increasing the damping to 24 kNs/m, initial differential wear has nearly negligible fluctuation amplitude and corrugation cannot grow in this case. These results suggest that increasing fastening longitudinal damping can effectively attenuate the initial excitation and reduce the track corrugation propensity.

5 Influence of train speeds on corrugation features

This section analyses the influence of train speeds on corrugation features. Different train speeds from 20 to 300 km/h have been simulated with RPM6. Figure 14 shows the influence of train speeds on the wavelengths and frequencies of longitudinal dynamic force, which determine the final corrugation wavelengths and frequencies [23]. When train speed decreases considerably from 140 to 90 and 40 km/h, the major wavelength with the highest magnitude changes relatively slightly from 28.6 to 21.8 and 23.8 mm, see Fig. 14a. This agrees with the field observation that the corrugation wavelength varies little with train speeds. The reason behind this phenomenon is the 'frequency selection and jump' [23], as shown in Fig. 14b and further explained below. At 140 km/h, the wheel–rail resonance 'selects' to occur mainly at 1360 Hz, causing a corrugation wavelength of 28.6 mm. When train speeds decrease, this resonance frequency 'jumps' largely to 1147 Hz at 90 km/h (a wavelength of 21.8 mm) and 467 Hz at 40 km/h (a wavelength of 23.8 mm), leading to a relatively small variation of the corrugation wavelength. Besides, it is worth noting that train speeds will also influence the resonance amplitude; e.g. 90 km/h is the smallest and 40 km/h is the largest in these three cases.

To better understand the influence of train speeds on corrugation, Fig. 15 shows the simulation results of fifteen cases with different speeds between 20 and 300 km/h. Figure 15a shows that the corrugation wavelength overall falls between 20 and 60 mm, and seems insensitive to the variation of train speeds. However, Fig. 15b shows that corrugation only occurs at nine major frequencies of about 240, 470, 675, 970, 1150, 1360, 1560, 2030, and 3000 Hz (indicated by dashed lines), respectively, from 20 to 300 km/h. These frequencies correspond to rail longitudinal compression modes [24], see some examples in Fig. 15d–g. With increasing train speeds, the wheel–rail resonance occurs at higher frequencies of rail longitudinal modes due to the frequency selection and jump, leading to an apparent 'wavelength-fixing' phenomenon [23]. The 'wavelength-fixing' mechanism of corrugation is in essence the frequency selection of different rail longitudinal compression modes under a certain train speed.

Once the corrugation is initiated by the rail longitudinal modes, it will, in turn, excite the vehicle–track system together with the initial excitation. The vertical modes will be excited and play an increasingly important role in the corrugation growth [23]. The excited vertical mode frequencies depend on the corrugation frequencies, which are dominated by the rail longitudinal modes. Therefore, different train speeds are expected to also cause the frequency selection and jump of the rail vertical modes, which is in essence the result of the frequency selection and jump of the rail longitudinal modes.

Figure 15c shows the maximum PSD magnitudes of longitudinal dynamic force with different train speeds. It can be seen that the train speed of 50 km/h causes the strongest wheel–rail resonance, and corrugation could be the easiest to initiate. However, those of 70 and 80 km/h are at a

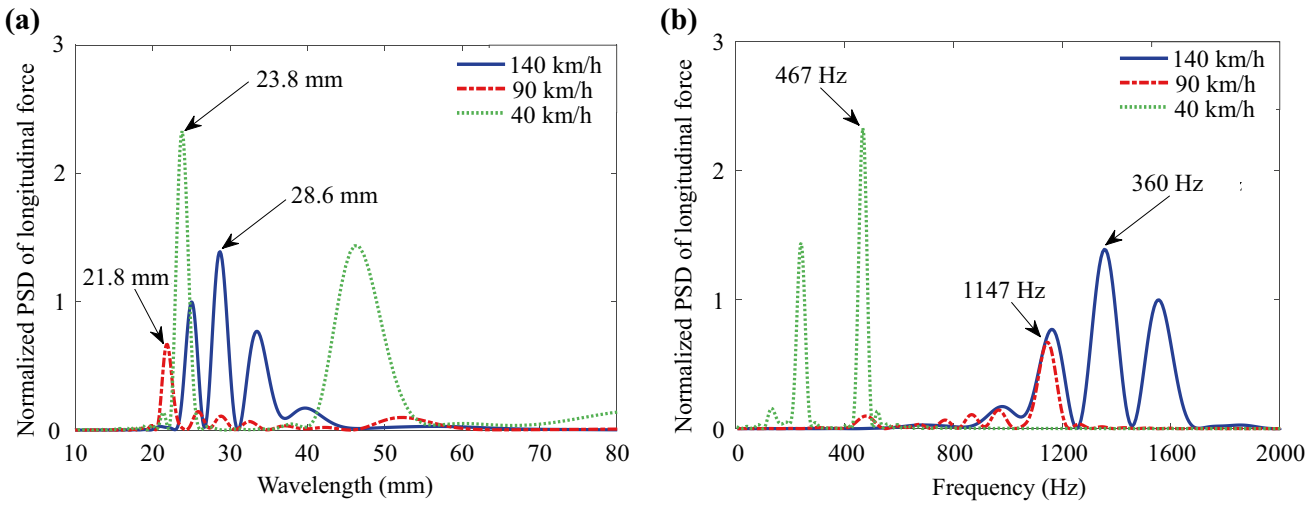

Fig. 14 The influence of train speeds on the longitudinal dynamic force and corrugation in the **a** wavelength and **b** frequency domains

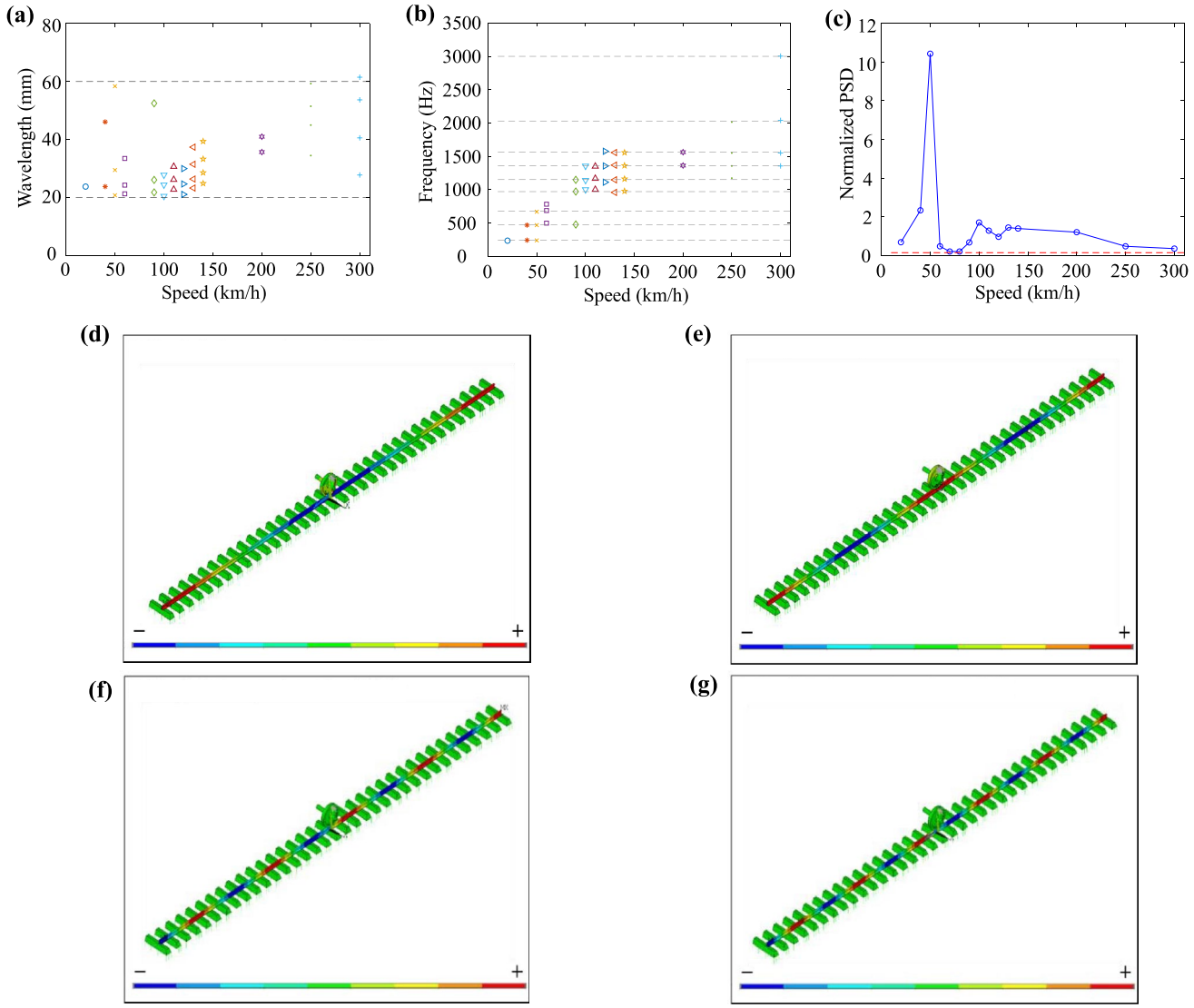

Fig. 15 The influence of train speeds on the **a** wavelength, **b** frequency, and **c** magnitudes of the longitudinal dynamic forces, and rail longitudinal compression modes at **d** 260 Hz, **e** 495 Hz, **f** 1170 Hz, and **g** 1420 Hz

small level similar to that with the nominal fastening RPM3 (indicated by the red dashed line), and corrugation could be less likely to initiate in these scenarios. This result indicates that eigenmodes of vehicle–track systems will not always cause strong wheel–rail resonance and corrugation, and the resonance occurrence and intensity depend largely on traffic speeds.

6 Discussion

In this work, fourteen fastening models were employed to investigate their influences on corrugation formation. These fastening models correspond to different service stages of fastenings in the field track, from nominal (i.e. RPM1) to severely worn conditions (i.e. RPM2). With some models, corrugation can consistently initiate and grow, while some cannot. Based on these results, we can obtain a better understanding of the corrugation formation mechanism and gain insights into corrugation mitigation.

6.1 Comparison of numerical simulations with field corrugation observations

Extensive numerical simulations have been performed and analysed above. To relate these numerical simulations to the field corrugation, some observations and measurements in the field are presented in this section. The monitored track with corrugations was a straight section of the Dutch railway network in Steenwijk with a maximum operation speed of

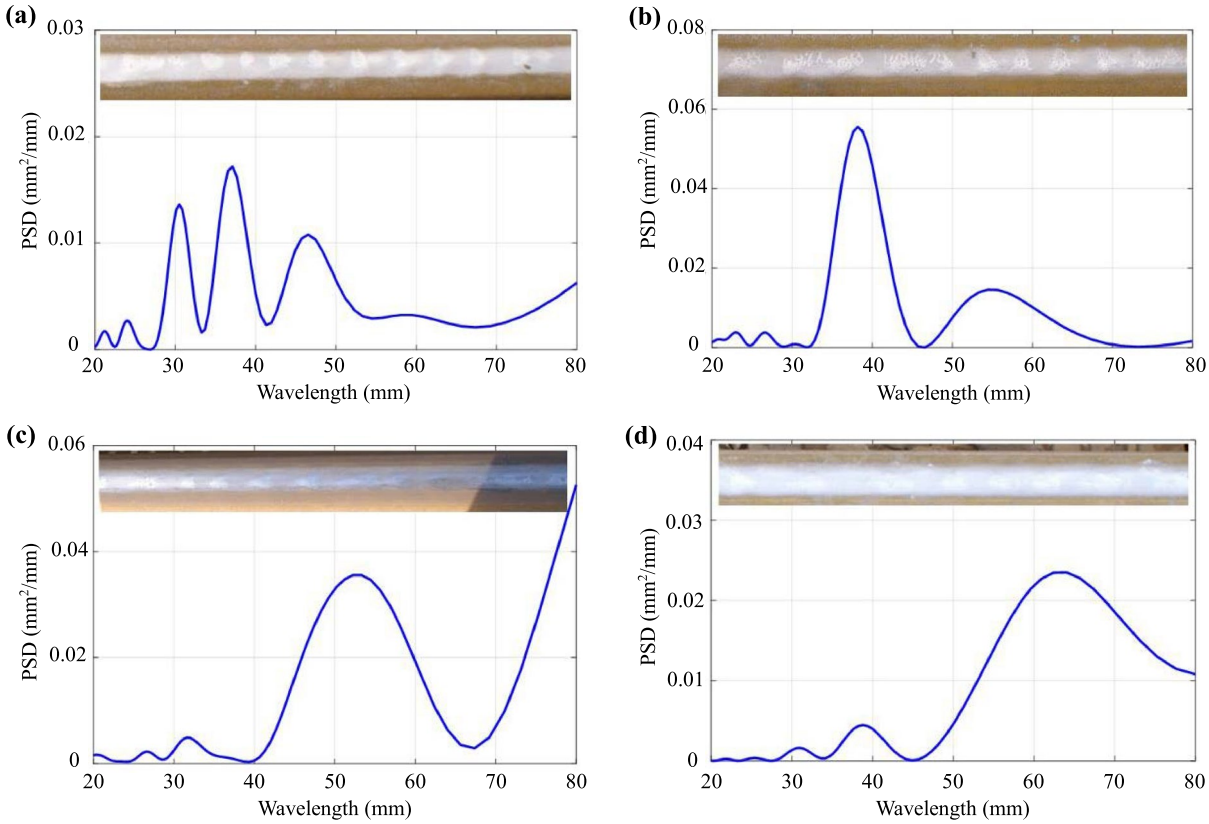

Fig. 16 Four examples of rail corrugation observed the in Dutch railway: **a** corrugation with multiple wavelengths of 30, 37, and 47 mm; **b** corrugation with a major wavelength at 38 mm; **c** corrugation with a major wavelength at 52 mm; **d** corrugation with a major wavelength at 64 mm

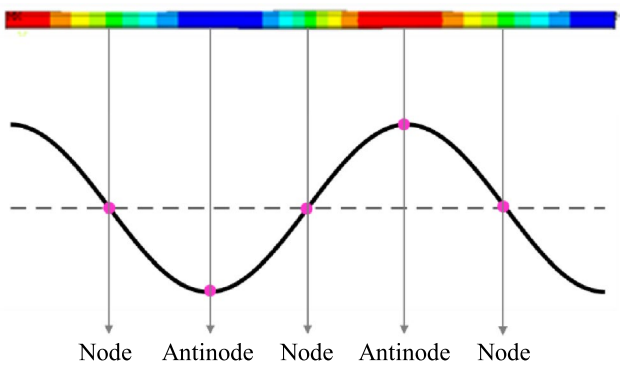

Fig. 17 A longitudinal compression mode at 1545 Hz of a 5-m long free rail

140 km/h. The track is ballasted with duo-block sleepers and Deenik fastening clips. The corrugation geometry was measured using RAILPROF over 1 m.

First, it is observed that corrugation is not everywhere even after more than 20 years of service, but only occurs at some particular locations. This indicates that in normal conditions without necessary initial excitation, corrugation will not initiate, agreeing with the numerical simulation with the fastening model RPM1. Moreover, it can be inferred that the stochastic roughness on the rail and wheel surface is not decisive to corrugation formation; otherwise, corrugation will be everywhere, which is the reason why the stochastic roughness is not considered in the current study.

Second, with a mainline traffic speed of about 140 km/h, field observations indicate that corrugation wavelengths vary largely from about 20 to 70 mm with the majority falling within 25–50 mm, see some examples in Fig. 16. This agrees well with our simulations with different fastening models. For instance, the major corrugation wavelength is about 25 mm with RPM3 (Fig. 9b), 50 mm with RPM9 (Fig. 10d), and 65 mm with RPM5 (Fig. 9d). Furthermore, if looking at the corrugation wavelengths reproduced with different fastening models (Figs. 9, 10, 11, 12, and 13), they fall between 25 and 50 mm in most cases. The numerical simulations also show that corrugation may have single (e.g. with RPM3 and RPM5) or multiple dominant wavelengths (e.g. with RPM 2 and RPM6), agreeing with the field observations in Fig. 16.

Overall, the simulation in this work can well explain the field corrugation in terms of the occurrence possibility and major wavelength components. It can also explain the field data with respect to the small variation between the

corrugation wavelength and train speed, detailed in Sect. 5. However, since the service states of the fastenings, e.g. railpad ageing and degradation, can be hardly evaluated only by field observations, we cannot directly relate the corrugation to fastenings in the current stage. Nevertheless, it has been demonstrated in recent work that fastening constraints can be effectively assessed by, e.g. field hammer tests [52] and axle box acceleration measurement [53]. Combining these methods with long-term field corrugation observations, it is possible to build up a direct relationship between field corrugation and the fastenings and more completely validate the numerical findings.

6.2 Insights into corrugation mitigation

Rail longitudinal compression modes are responsible for corrugation initiation, and hence, the suppression of these modes is helpful to mitigate corrugation. Figure 17 shows one example of a longitudinal compression mode at 1545 Hz of a free 5-m long rail. The term 'node' in the mode shape refers to a place where the rail does not move, and 'antinode' is used to describe a place with maximum displacement. The natural frequencies of longitudinal compression modes of a free rail can be predicted as follows [49]:

$$f = Nv_p/2L, \quad N = 1, 2, 3 \ldots, \tag{2}$$

where L is the length of the rail, and v_p is the phase velocity. The longitudinal compression wave is non-dispersive within 5000 Hz, with a constant phase velocity of around 5170 m/s [49].

In the field track, the rail is restricted by fastening systems. Figure 18 shows experimental results of rail longitudinal compression modes (the major peaks indicated by ★ and numbers) with and without fastenings by operating deflection shape (ODS) measurement. The minor peaks come from the mode coupling of the different directions, e.g. vertical bending modes. Detailed analysis can be found in [50]. Two types of railpads, harder Zw692-4 and softer FC9, were tested, which are commonly used in the mainline of the Dutch railway network. Compared to a free rail, the frequencies of longitudinal compression modes are shifted to higher values, and the corresponding vibration amplitude is significantly reduced under fastening constraint. For the softer FC9, the frequency shift and amplitude reduction are smaller than those of harder Zw692-4. These results qualitatively explain the effect of different fastening longitudinal constraints on corrugation features in Sects. 3 and 4. Despite the considerable attenuation by fastening constraint, longitudinal compression modes still have large vibration amplitude and show distinguishable peaks in Fig. 18.

To further suppress these modes, there are two possible approaches. One is to increase the fastening longitudinal damping. When the damping is sufficient to attenuate the longitudinal modes, corrugation cannot develop, as with RPM14 in Fig. 13. However, it should be noted that the damping capacity of railpads becomes weaker and even non-existent after long-term ageing and degradation, and corrugation can develop afterwards. A rail vibration absorber/damper might be a solution [54, 55], but its application requires information about the characteristic frequencies of corrugation. According to the analysis above, corrugation characteristic wavelengths/frequencies depend on the fastening parameters, which could cover a wide range (i.e. 600–2000 Hz) and make the vibration absorber/damper difficult to design and apply in the field.

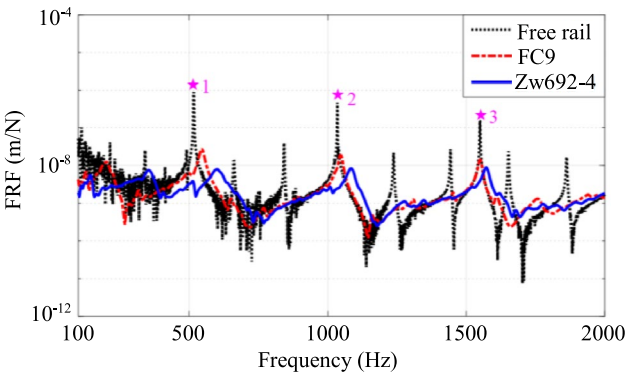

Fig. 18 Rail longitudinal compression modes in the free condition and under fastening constraint with two railpad types. The results are from [50]

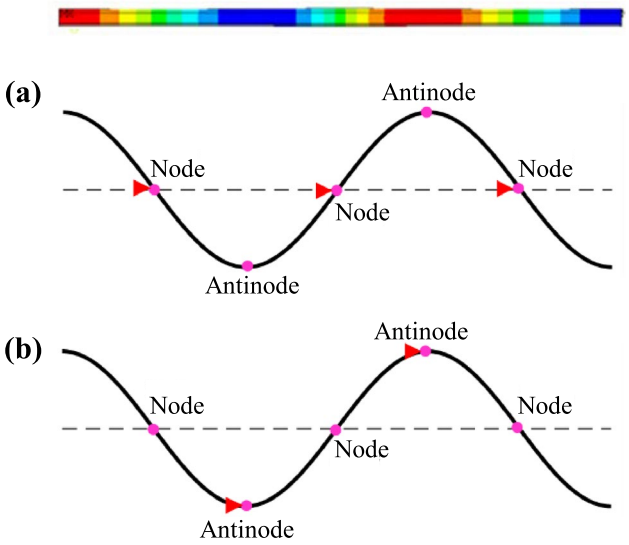

Fig. 19 Schematic drawing of two types of rigid constraint to the longitudinal compression mode: **a** rigid constraint to 'nodes'; **b** rigid constraint to 'antinode'

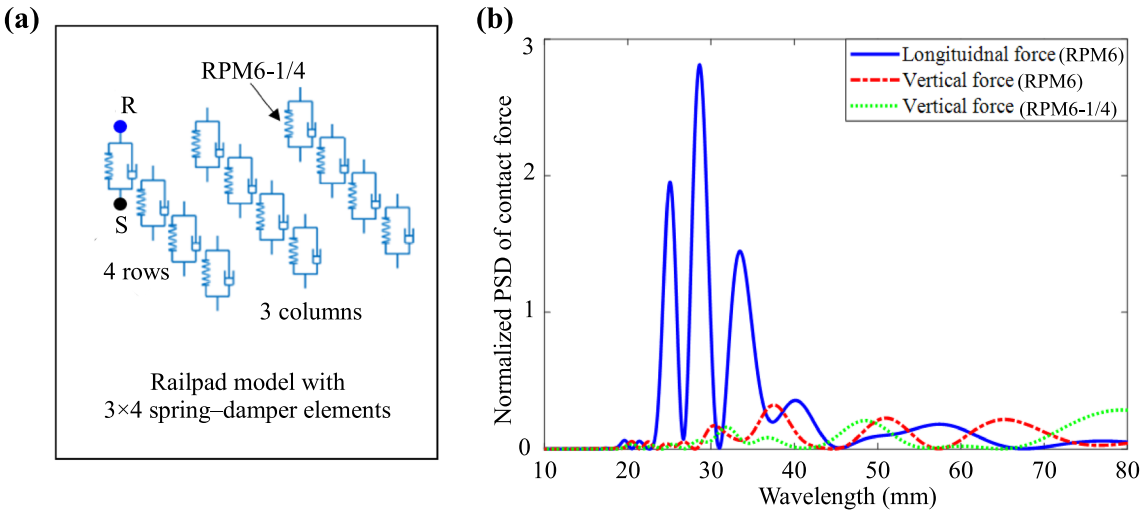

Fig. 20 The influence of vertical fastening stiffness on vertical contact force with RPM6: **a** schematic drawing of the vertical fastening stiffness reduction to 1/4 of the RPM6 nominal value; it should be noted that the stiffness of all 12 springs is evenly reduced to 1/4; **b** the influence of vertical fastening stiffness on vertical contact force. In this figure, the RPM6-1/4 means to reduce the vertical stiffness to 1/4 of the nominal value

Another approach is to increase the fastening longitudinal stiffness. One extreme condition of larger stiffness is the rigid constraint, like the fastening model RPM1. With RPM1, rail longitudinal compression modes are effectively suppressed, and corrugation can barely grow, as shown in Fig. 8a. Nevertheless, despite the longitudinal rigid constraint to the rail with RPM2 and RPM6, corrugation can still grow, indicating that longitudinal compression modes are not completely constrained. To explain these phenomena, Fig. 19 shows the schematic drawing of two types of rigid constraints to the longitudinal compression mode. When the rigid constraint is applied in the proximity of the 'nodes' of the mode shape, it has negligible influence on longitudinal compression modes, which could be the case of RPM2 and RPM6. When the rigid constraint is applied in the vicinity of the 'antinodes' of the mode shape, longitudinal compression nodes can be effectively suppressed, which could be the case of RPM1. This result provides an insight into the new fastening design for corrugation mitigation in future work.

6.3 Fastening modelling and parameters

It is proposed [23] that the degraded fastening model can serve as an effective initial excitation to the vehicle–track system to induce wheel–rail longitudinal resonance for corrugation initiation. This work confirms that fastening parameters and modelling play an important role in corrugation formation. The experimental verification using an innovative V-Track test rig in Ref. [25] also indicates that loose fastenings that simulate field fastening degradation can excite rail longitudinal vibration modes, induce longitudinal dynamic force, and cause corrugation. Since the rail longitudinal vibration modes are dominant for corrugation initiation, in this work, we mainly analyse the effect of longitudinal fastening constraint on corrugation formation. In reality, the fastening degradation will also change the vertical fastening stiffness, which may cause fluctuation of contact forces, differential wear, and corrugation. Figure 20 shows the influence of different vertical fastening stiffness on the vertical contact force with RPM6. When the vertical fastening stiffness reduces to 1/4 of the nominal value, some frequency shifts are observed in the PSD of the vertical contact force, which should be caused by the change of vertical eigenmodes of the vehicle–track system. However, the decrease in vertical stiffness does not considerably increase the fluctuation amplitude of the vertical force, and the fluctuation is much less than that of the longitudinal force. The magnitude of dynamic forces determines if the corrugation can initiate. This result may indicate that corrugation initiation is not so sensitive to the vertical fastening constraint as the longitudinal one in the current case.

In the current 3D FE vehicle–track dynamic model, the fastening elasticity is modelled by the linear spring–damper elements, whose parameters are identified by fitting the simulated track dynamic behaviours to the field hammer tests. Although this is a simplification of the real fastening constraints, it has been proved to be appropriate for representing track dynamics [43] and wheel–rail dynamic interaction [37, 42, 48]. In the literature, there are other advanced fastening models to consider the nonlinearity of the fastening constraints, such as Prony series model [30] and fractional derivative model [36, 56], and other approaches to determine nonlinear fastening parameters, such as dynamic mechanical analysis [30]. Future research will be

performed to consider the material nonlinearity in the model and validate the 3D FE model with various fastening configurations and parameters.

7 Conclusions and future work

Employing a 3D FE vehicle–track interaction model, a parametric investigation of fastenings was performed in this paper to better understand the corrugation formation mechanism and gain insight into its mitigation by fastening design. Fastening models with different configurations, boundary conditions, and parameters, representing different service stages of fastenings in the field, were built up and analysed. In addition, the influence of train speeds on corrugation features was studied. The simulation can well explain the field corrugation in terms of the occurrence possibility and major wavelength components.

The understanding of the corrugation formation mechanism is summarised as follows:

(1) Fastening parameters and modelling play an important role in corrugation formation. To better understand the corrugation features in the field and reliably predict corrugation in the simulation, it is suggested to carefully examine the service stages of fastenings to determine appropriate parameters.
(2) The variation of fastening constraint in the longitudinal direction (i.e. the number of columns significantly influences the corrugation formation and features). The absence of inner fastening constraint in the lateral direction (i.e. 2nd and 3rd rows) seems a preferred condition for the formation of relatively longer-wavelength corrugation.
(3) The fastening longitudinal constraint to the rail is the major factor that determines the corrugation formation because the rail longitudinal modes, which are responsible for corrugation initiation, are a type of compression/rarefaction vibration in the longitudinal direction. The fastening vertical and lateral constraints influence the spatial distribution and wavelength components of corrugation.
(4) Larger longitudinal stiffness of fastenings shifts the major wavelength components of corrugation to the shorter ones with significantly reduced amplitude. Larger longitudinal damping reduces the corrugation amplitude without changing the wavelength components.
(5) Limiting corrugation amplitude is dependent on the intensity of the initial excitation, and the resulting fluctuation amplitude of longitudinal dynamic contact force and initial differential wear.
(6) The small variation between the corrugation wavelength and train speeds is caused by frequency selection and jump between rail longitudinal compression modes.

Insights are gained for the corrugation mitigation by fastening design and summarised as follows:

(1) The strengthening of fastening constraint in the longitudinal direction helps to mitigate corrugation. Meanwhile, the inner fastening constraint in the lateral direction is necessary for corrugation mitigation.
(2) The increase in fastening longitudinal stiffness and damping can reduce the vibration amplitudes of longitudinal compression modes, and thus reduces the track corrugation propensity.
(3) To effectively mitigate corrugation, fastening constraints should be applied in the proximity of the 'antinodes' of the longitudinal compression mode shape instead of the 'nodes'.

Future work will focus on the new design of fastening systems, which can effectively suppress rail longitudinal compression modes, and hence mitigate or even eliminate corrugation in the track.

Acknowledgements The first author thanks China Scholarship Council for support.

References

1. Grassie S, Kalousek J (1993) Rail corrugation: characteristics, causes and treatments. Proc Inst Mech Eng Part F J Rail Rapid Transit 207(16):57–68
2. Deng X, Qian Z, Li Z et al (2018) Investigation of the formation of corrugation-induced rail squats based on extensive field monitoring. Int J Fatigue 112:94–105
3. Han J, Xiao X, Wu Y et al (2018) Effect of rail corrugation on metro interior noise and its control. Appl Acoust 130:63–70
4. Xin T, Wang S, Gao L et al (2020) Field measurement of rail corrugation influence on environmental noise and vibration: a case study in China. Measurement 164:108084
5. Neilsen J (1999) Evolution of rail corrugation predicted with a non-linear wear model. J Sound Vib 227(5):915–933

6. Meehan P, Bellette P, Batten R et al (2009) A case study of wear-type rail corrugation prediction and control using speed variation. J Sound Vib 325(1–2):85–105
7. Vuong T, Meehan P, Eadie D et al (2011) Investigation of a transitional wear model for wear and wear-type rail corrugation prediction. Wear 271(1–2):287–298
8. Correa N, Vadillo E, Santamaria J et al (2016) A versatile method in the space domain to study short-wave rail undulatory wear caused by rail surface defects. Wear 352–353:196–208
9. Zhao X, Zhang P, Wen Z (2019) On the coupling of the vertical, lateral and longitudinal wheel–rail interactions at high frequencies and the resulting irregular wear. Wear 430–431:317–326
10. Cui X, He Z (2021) Huang B et al Study on the effects of wheel–rail friction self-excited vibration and feedback vibration of corrugated irregularity on rail corrugation. Wear 477:203854
11. Li W, Zhou Z, Zhao X, Wen Z et al (2023) Formation mechanism of short-pitch rail corrugation on metro tangent tracks with resilient fasteners. Veh Syst Dyn 61(6):1524–1547
12. Hempelmann K, Knothe K (1996) An extended linear model for the prediction of short pitch corrugation. Wear 191:161–169
13. Muller S (1999) A linear wheel–track model to predict instability and short pitch corrugation. J Sound Vib 227(5):899–913
14. Hiensch M, Nielsen JC, Verheijen E (2002) Rail corrugation in The Netherlands—measurements and simulations. Wear 253(1–2):140–149
15. Grassie S (2009) Rail corrugation: characteristics, causes, and treatments. Proc Inst Mech Eng Part F J Rail Rapid Transit 223(6):581–596
16. Afferrante L, Ciavarella M (2009) Short-pitch rail corrugation: a possible resonance-free regime as a step forward to explain the "enigma"? Wear 266(9–10):934–944
17. Oostermeijer K (2008) Review on short pitch rail corrugation studies. Wear 265(9–10):1231–1237
18. Wang Y, Wu T (2020) The growth and mitigation of rail corrugation due to vibrational interference between moving wheels and resilient track. Veh Syst Dyn 58(8):1257–1284
19. Wu T, Thompson D (2005) An investigation into rail corrugation due to micro-slip under multiple wheel/rail interactions. Wear 258(7–8):1115–1125
20. Ma C, Gao L, Xin T et al (2021) The dynamic resonance under multiple flexible wheelset–rail interactions and its influence on rail corrugation for high-speed railway. J Sound Vib 498:115968
21. Robles R, Correa N, Vadillo EG et al (2023) Comprehensive efficient vertical and lateral track dynamic model to study the evolution of rail corrugation in sharp curves. J Sound Vib 545:117448
22. Li S, Li Z, Núñez A et al (2017) New insights into the short pitch corrugation enigma based on 3D-FE coupled dynamic vehicle–track modeling of frictional rolling contact. Appl Sci 7(8):807
23. Li Z, Li S, Zhang P, Núñez A et al (2022) Mechanism of short pitch rail corrugation: initial excitation and frequency selection for consistent initiation and growth. Int J Rail Transp 12(1):1–36
24. Zhang P, Li S, Li Z (2022) Short pitch corrugation mitigation by rail constraint design. Int J Mech Sci 243:108037
25. Zhang P, Li Z (2023) Experimental study on the development mechanism of short pitch corrugation using a downscale V-Track test rig. Tribol Int 180:108293
26. Zhang H, Liu W, Liu W et al (2014) Study on the cause and treatment of rail corrugation for Beijing metro. Wear 317(1–2):120–128
27. Liu W, Zhang H, Liu W et al (2018) Experimental study of the treatment measures for rail corrugation on tracks with egg fasteners in the Beijing metro. Proc Inst Mech Eng Part F J Rail Rapid Transit 232(5):1360–1374
28. Eldred LB, Baker WP, Palazotto AN (1995) Kelvin–Voigt versus fractional derivative model as constitutive relations for viscoelastic materials. AIAA J 33(3):547–550
29. Ripke B (1995) Hochfrequente Gleismodellierung und Simulation der Fahrzeug-Gleis-Dynamik unter Verwendung einer nichtlinearen Kontaktmechanik. VDI-Verlag, Düsseldorf
30. Oregui M, De Man A, Woldekidan M et al (2016) Obtaining railpad properties via dynamic mechanical analysis. J Sound Vib 363:460–472
31. Fenander A (1998) A fractional derivative railpad model included in a railway track model. J Sound Vib 212(5):889–903
32. Xu J, Li J (2016) Stochastic dynamic response and reliability assessment of controlled structures with fractional derivative model of viscoelastic dampers. Mech Syst Signal Process 72–73:865–896
33. Oregui M, Li Z, Dollevoet R (2015) An investigation into the modeling of railway fastening. Int J Mech Sci 92:1–11
34. Thompson D, Jones C, Wu T et al (1999) The influence of the non-linear stiffness behaviour of rail pads on the track component of rolling noise. Proc Inst Mech Eng Part F J Rail Rapid Transit 213(4):233–241
35. Egana J, Vinolas J, Seco M (2006) Investigation of the influence of rail pad stiffness on rail corrugation on a transit system. Wear 261(2):216–224
36. Wei K, Wang F, Wang P et al (2017) Effect of temperature-and frequency-dependent dynamic properties of rail pads on high-speed vehicle–track coupled vibrations. Veh Syst Dyn 55(3):351–370
37. Zhao X, Li Z, Dollevoet R (2014) Influence of the fastening modeling on the vehicle–track interaction at singular rail surface defects. J Comput Nonlinear Dyn 9(3):031002
38. Knothe KL, Grassie SL (1993) Modelling of railway track and vehicle/track interaction at high frequencies. Veh Syst Dyn 22(3–4):209–262
39. Zhao X, Li Z (2011) The solution of frictional wheel–rail rolling contact with a 3D transient finite element model: validation and error analysis. Wear 271(1–2):444–452
40. Yang Z, Deng X, Li Z (2019) Numerical modeling of dynamic frictional rolling contact with an explicit finite element method. Tribol Int 129:214–231
41. Benson DJ, Hallquist JO (1990) A single surface contact algorithm for the post-buckling analysis of shell structures. Comput Methods Appl Mech Eng 78(2):141–163
42. Yang Z, Boogaard A, Chen R et al (2018) Numerical and experimental study of wheel–rail impact vibration and noise generated at an insulated rail joint. Int J Impact Eng 113:29–39
43. Oregui M, Li Z, Dollevoet R (2016) An investigation into the vertical dynamics of tracks with monoblock sleepers with a 3D finite-element model. Proc Inst Mech Eng Part F J Rail Rapid Transit 230(3):891–908
44. Yang Z, Zhang P, Wang L (2021) Wheel–rail impact at an insulated rail joint in an embedded rail system. Eng Struct 246:113026
45. Li Z, Zhao X, Esveld C et al (2008) An investigation into the causes of squats—correlation analysis and numerical modeling. Wear 265(9–10):1349–1355
46. Li Z, Dollevoet R, Molodova M et al (2011) Squat growth—some observations and the validation of numerical predictions. Wear 271(1–2):148–157
47. Sadeghi J, Seyedkazemi M, Khajehdezfuly A (2020) Nonlinear simulation of vertical behavior of railway fastening system. Eng Struct 209:110340
48. Molodova M, Li Z, Núñez A et al (2014) Validation of a finite element model for axle box acceleration at squats in the high frequency range. Comput Struct 141:84–93
49. Zhang P, Li S, Núñez A et al (2021) Multimodal dispersive waves in a free rail: Numerical modeling and experimental investigation. Mech Syst Signal Process 150:107305
50. Zhang P, Li S, Núñez A et al (2021) Vibration modes and wave propagation of the rail under fastening constraint. Mech Syst Signal Process 160:107933

51. Kalousek J, Johnson K (1992) An investigation of short pitch wheel and rail corrugations on the Vancouver mass transit system. Proc Inst Mech Eng Part F J Rail Rapid Transit 206(2):127–135
52. Shen C, Dollevoet R, Li Z (2021) Fast and robust identification of railway track stiffness from simple field measurement. Mech Syst Signal Process 152:107431
53. Shen C, Zhang P, Dollevoet R et al (2023) Evaluating railway track stiffness using axle box accelerations: a digital twin approach. Mech Syst Signal Process 204:110730
54. Croft B, Jones C, Thompson D (2009) Modelling the effect of rail dampers on wheel–rail interaction forces and rail roughness growth rates. J Sound Vib 323(1–2):17–32
55. Wu T (2011) Effects on short pitch rail corrugation growth of a rail vibration absorber/damper. Wear 271(1–2):339–348
56. Yang F, Zhang P, Wang Y et al (2023) Refined nonlinear fractional derivative model of vehicle–track coupling dynamics. Int J Non-Linear Mech 154:104444